Fluorine Substitution in Magnesium Hydride as a Tool for Thermodynamic Control

Terry D. Humphries,*[a] Jack Yang,[b,c] Richard A. Mole,[b] Mark Paskevicius,[a] Julianne E. Bird,[a] Matthew R. Rowles,[a,d] Mariana S. Tortoza,[a] M. Veronica Sofianos,[a] Dehong Yu,[b] Craig. E. Buckley[a]

[a] Physics and Astronomy, Fuels and Energy Technology Institute, Curtin University, GPO Box U1987, Perth, WA 6845, Australia

[b] Australian Nuclear Science and Technology Organisation, Locked Bag 2001, Kirrawee DC NSW 2232 Australia

[c] School of Material Science and Engineering & Advanced Materials and Manufacturing Futures Institute, University of New South Wales, Sydney, New South Wales, 2052 Australia

[d] John De Laeter Centre, Curtin University, GPO Box U1987, Perth, WA 6845, Australia

ABSTRACT: Metal hydrides continue to vie for attention as materials in multiple technological applications including hydrogen storage media, thermal energy storage (TES) materials and hydrogen compressors. These applications depend on the temperature at which the materials desorb and reabsorb hydrogen. Magnesium hydride is ideal as a TES, although its practical operating temperature is capped at ~450 °C due to material degradation and high operating pressure. Fluorine substitution for hydrogen in magnesium hydride has previously been shown to increase the operating temperature of the metal hydride whilst limiting degradation, although full characterisation is required before technological application can be ensured. The present study characterises $Mg(H_xF_{1-x})_2$ solid solutions (x = 1, 0.95, 0.70, 0.85, 0.50, 0) by inelastic neutron spectroscopy, powder X-ray diffraction and thermal conductivity measurements, with the results being verified by density functional theory. For each experiment, a clear trend is observed throughout the series of solid-solutions, showing the possibility of tuning the properties of MgH_2. As F^- substitution increases, the average Mg−H(F) bond distance elongates along the axial positions of the Mg−H(F) octahedra. Overall this leads to an increase in Mg−H bond strength and thermal stability, improving the viability of Mg−H−F as potential TES materials.

1. INTRODUCTION

For the global energy network to convert to a green hydrogen economy, four challenges must be met: (i) hydrogen production must primarily be from a renewable source; (ii) utilisation must be optimised including refuelling station infrastructure and fuel cells; (iii) hydrogen distribution must be safe and cost effective; and (iv) storage media for the hydrogen must be developed. There are a number of ways that hydrogen can be stored, including as a gas, cryogenic liquid, or chemically, e.g. within a metal hydride or ammonia.[1, 2] Metal hydrides, and in particular magnesium-based hydrides, have received enormous attention over the last 60 years for their potential as hydrogen storage materials.[3-6] This has largely been due to the relatively high abundancy of magnesium metal in the Earth's crust and its relatively low cost of extraction.[5] In addition, magnesium hydride has been shown to be highly reversible when used as a hydrogen storage material at a modest temperature. The binary hydride (MgH_2) has a theoretical hydrogen storage capacity of 7.7 wt% H_2, but due to its relatively high enthalpy of hydrogen desorption of 74 kJ/mol H_2 and entropy of 133 J/K/mol.H_2, its operational temperatures are limited to only 300 °C at 1 bar H_2 pressure,[7] ensuring that MgH_2 will never find technological application as a reversible fuel store for vehicular applications, as temperatures of ~85 °C are preferred.[8] As such, MgH_2 has alternatively been considered as a material for thermal energy storage (TES) applications, such as storing heat from the sun to use at periods of weak solar irradiation, as a thermal battery. However, it cannot operate above ~450 °C due to the tendency for magnesium to agglomerate, thus reducing its long term hydrogen storage capacity and also reducing the reaction kinetics.[9]

Many studies have been published in which issues with kinetics and agglomeration have been addressed by innovative approaches including nano-sizing, infiltration into porous scaffolds, and the incorporation of additives, including TiB_2 as a particle refinement agent.[4, 5, 9, 10] All of these methods have proven successful in some regard and combinations of methods seem to be ideal. Recently, fluoride substitution for hydrogen in the Mg−H system has been reported in which solid–solutions are synthesised by ball milling MgH_2 and MgF_2 in various ratios and also studied by density functional theory calculations.[10-12] Fluorine substituted magnesium hydride solid solutions, $Mg(H_xF_{1-x})_2$, were deemed to be stabilised compared to pure MgH_2 and attributed to the positive enthalpy of mixing ($\Delta H_{mix} > 0$).[11]

The decomposition temperature of $Mg(H_xF_{1-x})_2$ was determined *via* simultaneous differential scanning calorimetry – thermogravimetry (DSC-TGA) and powder X-ray diffraction (XRD) experiments. In addition, the thermodynamics of hydrogen release for $Mg(H_{0.85}F_{0.15})_2$ were determined to be 73.6 kJ/mol.H_2 and 131.2 J/K/mol.H_2 close to that of pure MgH_2. Interestingly, this material was shown to cycle at high temperatures, between 425 and 480 °C. Despite the determination of these physical properties, little else is known regarding the fluorine substituted materials, although a smattering of analysis techniques have been used to study the physical properties of pure MgH_2 (other than

thermodynamics and kinetics) including powder neutron and X-ray diffraction,[13] NMR spectroscopy,[14, 15] vibrational spectroscopy[16-20] and thermal conductivity.[21, 22]

With $Mg(H_{0.85}F_{0.15})_2$ showing favourable operating temperatures as a thermal energy storage material, additional exploration of the physical properties for $Mg(H_xF_{1-x})_2$ solid solutions have herein been undertaken by inelastic neutron spectroscopy, powder X-ray diffraction and thermal conductivity measurement. In addition, DFT calculations have been performed to corroborate the inelastic neutron spectroscopy and powder X-ray diffraction results. This has allowed a full comparison on the stability of fluorine substitution in magnesium hydride.

2. EXPERIMENTAL SECTION

2.1. Sample Preparation All manipulations of chemicals were undertaken in an argon atmosphere using an Mbraun Unilab glovebox to prevent air exposure and to minimise oxygen (O_2 < 1 ppm) and water (H_2O < 1 ppm) contamination. $Mg(H_xF_{1-x})_2$ (x = 1, 0.95, 0.85, 0.70, 0.50, 0) samples were prepared by ball milling (BM) various ratios of MgH_2 and MgF_2 (Sigma-Aldrich, >99.99 %) at room temperature. MgH_2 powder (95 wt% purity from Rietveld refinement of X-ray diffraction data) was synthesised by annealing Mg powder (Aldrich, >99 %) at 400 °C under 30 bar hydrogen pressure for 18 hours. The full synthesis description is found in ref [10]. BM of MgH_2 and MgF_2 was undertaken at 400 rpm for 40 hours in an Across International Planetary Ball Mill (PQ-N04) with a ball-to-powder mass ratio of 50:1 using stainless steel vials and balls (6 and 8 mm in diameter) under an Ar atmosphere. After milling, samples were annealed under a hydrogen atmosphere of 60 bar at 450 °C for a period of 90 hours to form solid solutions.

2.2. Synchrotron X-ray Characterisations *S*ynchrotron powder X-ray diffraction (SR-XRD) was performed on the Powder Diffraction beamline at the Australian Synchrotron in Melbourne, Australia.[23] Without exposure to air, the $Mg(H_xF_{1-x})_2$ powders were loaded into borosilicate or quartz capillaries (outer diameter 0.7 mm, wall thickness 0.01 mm) that were then, using graphite ferrules, mounted in 1/16" tube fittings connected to a gas manifold. One-dimensional SR-XRD patterns (monochromatic X-rays with λ = 1.0003896 or 0.8263076 Å) were collected using a Mythen microstrip detector[24] with an exposure time of 54 s per pattern. The wavelength and line shape parameters were calibrated against an external standard of LaB_6 (NIST SRM660c). The capillaries were continuously oscillated through 120° during exposure to improve powder averaging. Diffraction patterns were quantitatively analysed using the Rietveld refinement method[25, 26] with TOPAS software (Bruker-AXS).[27]

2.3. Inelastic Neutron Scattering Characterisations Inelastic neutron scattering (INS) data were collected using the Pelican cold-neutron time-of-flight spectrometer located at the OPAL reactor Lucas Heights, Australia. Samples were mounted in rectangular, flat plate, aluminium sample cans, with the thickness optimised for a 10 % scatter, i.e. to minimise multiple scattering. The sample cans were mounted at 45° to the incident beam and placed in a vacuum chamber at room temperature. The instrument was aligned for 4.69 Å neutrons and the choppers were run in a time focusing configuration at either 100 or 200 Hz. The resolution at the elastic line was 135 μeV. An empty can was subtracted to determine the background contribution and the data was normalised using data collected with a vanadium standard that had the same geometry as the sample can. All data manipulations were performed using the freely available software Lamp.[28] Data were collected as $S(Q,\omega)$ [i.e. scattering cross-section as a function of scattering wavevectors (Q) and phonon frequency (ω)], and these were transformed to a generalised density of states using formula (1), where k_b is Boltzmann's constant, T is temperature and $\hbar$ is the reduced Planck's constant.[29]

$$g(\omega) = \int \frac{\omega}{Q^2} S(Q,\omega)(1 - e^{\frac{-\hbar\omega}{k_b T}})\, \mathrm{d}Q \qquad (1)$$

2.4. Thermal Property Characterisation The thermal conductivity (λ_{TC}), thermal diffusivity (k) and the heat capacity per unit volume (C) of 5 ratios of F^- and H^- in $Mg(H_xF_{1-x})_2$ were measured using a TPS 500S (Hot Disk, Thermtest). Measurements were undertaken in an argon atmosphere at a constant ambient temperature, measured by a K type thermocouple. 1.5 g of $Mg(H_xF_{1-x})_2$ (x = 1, 0.95, 0.85, 0.70, 0.50, 0) were pressed in a die (13 mm diameter) using a manual hydraulic press (370 MPa of pressure for 5 minutes). A nickel double-spiral sensor (2 mm radius), laminated by electrically insulating Kapton was firmly clamped co-centrically between the pellets. 10 measurements per sample were conducted, with 15 minutes in between each measurement to allow the sample and sensor to cool.

2.5. First-Principle Calculations Density Functional Theory (DFT) based lattice dynamic calculations were performed to complement the INS measurements in order to better understand the stability and bonding in $Mg(H_xF_{1-x})_2$ systems. All DFT calculations were performed with VASP[30] under a generalised gradient approximation (GGA) using the Perdew-Burke-Ernzerhof (PBE) functionals together with the projector augmented wave (PAW) potentials.[31, 32] The energy cut-off for planewave expansion was set to 500 eV. The minimum-energy configurations for MgH_2 and MgF_2 were optimised with a dense ($15 \times 15 \times 15$) Monkhorst-Pack K-point mesh. For all subsequent phonon calculations, geometry optimisations were relaxed with an energy convergence of 10^{-7} eV and forces less than 10^{-6} eV/atom.

In order to account for the statistically disordered nature of F-substitution in MgH_2, all unique configurations of F-substituted MgH_2 supercells were sampled for calculating the corresponding thermodynamic stabilities and phonon density of states (DOS). Here, $Mg(H_xF_{1-x})_2$ at different concentrations (x = 0.95, 0.90, 0.85, 0.80, 0.75, 0.70 and 0.50) were simulated, which led to a total number of configurations of 34, 33, 30, 27, 26, 2, 2, respectively, for each nominated F concentration. Supercells of sizes ($1 \times 1 \times 1$) [for x = 0.50], ($5 \times 1 \times 1$) and ($1 \times 1 \times 5$) [for all other fluoride concentrations] were used with corresponding Monkhorst-Pack K-point meshes of ($6 \times 6 \times 9$), ($2 \times 6 \times 6$) and ($6 \times 6 \times 2$), respectively. Because MgH_2 adopts an orthorhombic lattice, supercell expansions along both the a and c axis were considered, as well as several possible unique F^- positions at a given x and supercell size. Thermodynamic stabilities (formation energies ΔE_f) for the substituted structure were modelled according to the following reaction:

$$Mg + xH_2 + (1-x)F_2 \rightarrow Mg(H_xF_{1-x})_2 \qquad (2)$$

Such that:

$$\Delta E_f = E[Mg(H_xF_{1-x})_2] - E[Mg] - xE[H_2] - (1-x)E[F_2] \qquad (3)$$

where E is the total energy from DFT calculations that contains both the ionic and electronic contributions.

Phonon DOS were calculated using a finite-displacement method as implemented in PHONOPY interfaced with VASP.[33] For $Mg(H_xF_{1-x})_2$ systems simulated with different supercells, the corresponding supercells and K-point meshes used in phonon calculations are summarised in Table 1.

The theoretically calculated phonon DOS were subsequently rescaled to consider the differences in the inelastic neutron scattering cross sections for different elements, as adopted by Bansal *et al.*,[34] where the neutron weighted DOS was calculated according to the following formula:

$$G = \sum_i \frac{\sigma_i}{m_i} g_i / N_{tot} \quad (4)$$

Here σ_i is either the coherent and incoherent neutron scattering cross-section for the i-th element, m_i is the corresponding atomic mass, g_i is the partial phonon density-of-states for the i-th element and N_{tot} is the total number of atoms in the supercell.[35] To effectively compare the phonon DOS across systems with different F concentrations, the phonon DOS at any given F concentration was averaged across all supercell configurations (N_{config}) considered at that concentration according to:

$$\overline{DOS(E)} = \frac{1}{N_{config}} \sum_{i=1}^{N_{config}} DOS_i(E) \quad (5)$$

No additional weighting parameter, such as the relative stabilities of different configurations (at a fixed F concentration) was used, because the differences in the calculated formation energies were almost negligible [see the Results section].

Table 1. Supercells and K-point meshes chosen for finite-displacement phonon calculations in VASP. Also shown is the $\boldsymbol{\Gamma}$-centred K-point grids used for phonon density-of-states integrations. Note that the supercell for phonon simulations were specified with respect to the supercells for calculating the substitution formation energies, not the primitive MgH_2 unit cell.

Defect supercell	Phonon supercell	Phonon K-point meshes	DOS integration grid
$1 \times 1 \times 1$	$3 \times 3 \times 3$	$2 \times 2 \times 3$	$20 \times 20 \times 20$
$5 \times 1 \times 1$	$1 \times 2 \times 2$	$2 \times 3 \times 3$	$10 \times 10 \times 10$
$1 \times 1 \times 5$	$2 \times 2 \times 1$	$3 \times 3 \times 2$	$10 \times 10 \times 10$

3. RESULTS AND DISCUSSION

3.1 Powder X-ray diffraction MgH_2 and MgF_2 both exist in the aristotypic rutile-type structure in space group $P4_2/mnm$. The lattice parameters measured after ball milling and annealing in this study are provided in Tables 2 and S1. These values agree with the literature values for MgH_2 and MgF_2, respectively.[36, 37] Despite the larger covalent character exhibited by MgH_2, the lattice parameters for MgH_2 are smaller than that observed for MgF_2.[12, 38, 39] Along with the fact that MgF_2 is significantly more stable than MgH_2, it is expected that Mg−F bonds be shorter. In fact, the axial Mg−H bond distances are 1.935973(6) Å compared to 1.98114(2) Å for the equivalent Mg−F bonds. Since F^- is highly electronegative, it will also form small covalent interactions between neighbouring F^-, which not only creates further stabilisation, but allows the Mg−F bond distance to increase.[12] This has been illustrated using electron density maps derived from theoretical calculations and X-ray diffraction measurements.[12, 39, 40] In MgF_2, electron density between the F^- atoms is observed, while most of the electron density has been withdrawn from the Mg^{2+} by the F^-. In MgH_2, some anisotropic charge distribution between the Mg and H and H atoms suggesting partial covalency.[12]

From Table 2 it can be seen that the greatest difference in lattice parameters is experienced in the a-axis of the unit cell with a 2.3 % decrease from MgF_2 to MgH_2 compared to 1.0 % in the c axis. This manifests into an overall decrease in unit cell volume of 5.4 % for MgH_2. The anisotropic nature of the lattice parameters points to the stability of the octahedral chains that run in the direction of the c-axis (Figure 1).[36] These chains, with four coplanar equatorial Mg−H(F) bonds, are connected via corner-sharing with four symmetrically equivalent chains, and are therefore quite stable. Thus there is only a 1.5 % change in the equatorial Mg−H(F) bonds compared to 2.3 % for the axial Mg−H(F) bonds.

Upon ball milling and annealing MgH_2 and MgF_2 in varying ratios (Table 2), $Mg(H_xF_{1-x})_2$ (x = 1, 0.95, 0.85, 0.70, 0.50, 0) was produced. No peak splitting was observed in the diffraction patterns, indicating that solid solutions were formed.[10] The lattice parameters, and by association, unit cell volume and bond distances increase with increasing F^- content, with each following a quadratic trend. Analysis was undertaken by quantitative Rietveld refinement of the SR-XRD data using Topas (illustrated in Figure S1 and Table S1).[27] Fifteen individual

Table 2. Structural properties of $Mg(H_xF_{1-x})_2$ (x = 1, 0.95, 0.85, 0.70, 0.50, 0) materials measured by SR-XRD at room temperature. Estimated standard deviations (esd's) are in parentheses**.**

	Lattice parameter (Å)		Mg−H(F) (Å)	
Sample name	**a**	**c**	**Axial**	**Equatorial**
MgH_2	4.51795(1)	3.02257(1)	1.935976(6)	1.966804(5)
	4.516(8)[a]	3.020(5)[a]	---	---
$Mg(H_{0.95}F_{0.05})_2$	4.52458(1)	3.02345(1)	1.946(3)	1.964(2)
$Mg(H_{0.85}F_{0.15})_2$	4.54284(1)	3.02982(1)	1.946637(4)	1.974028(4)
$Mg(H_{0.70}F_{0.30})_2$	4.56514(4)	3.04023(3)	1.95619(2)	1.98201(1)
$Mg(H_{0.50}F_{0.50})_2$	4.59225(3)	3.04441(2)	1.9716(8)	1.9860(5)
MgF_2	4.62337(5)	3.05214(5)	1.98114(2)	1.99700(2)
	4.6249(1)[b]	3.0520(1)[b]	---	---

[a] Ref [36], [b] Ref [37]

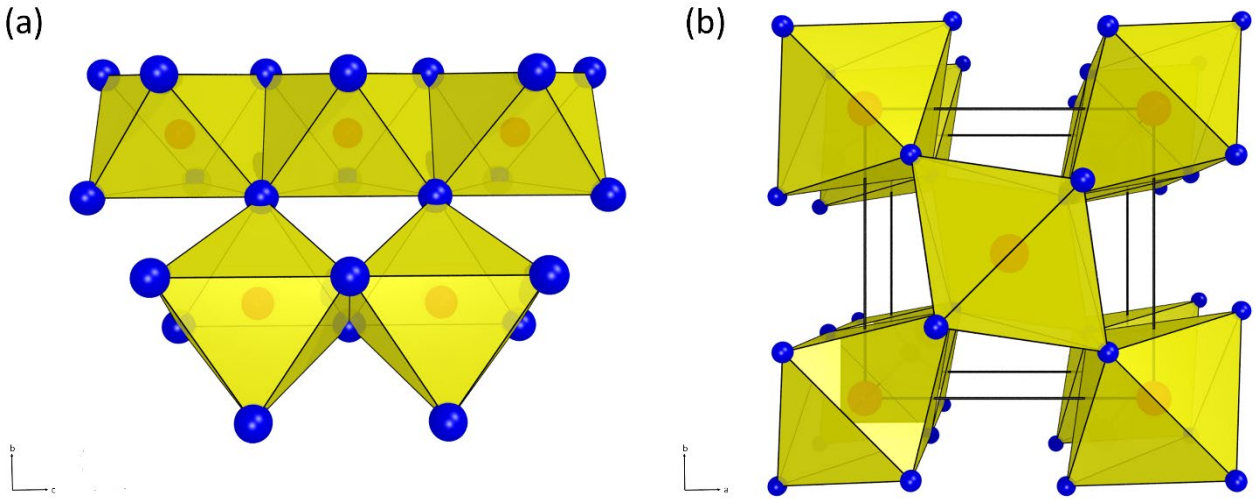

Figure 1. Representative views of $Mg(H_xF_{1-x})_2$; (a) Mg–H(F)$_6$ octahedral units viewed along the *a*-axis and (b) along the *c* axis. Mg atoms represented as red spheres, H(F) atoms as blue spheres and Mg–H(F)$_6$ octahedra represented with yellow faces.

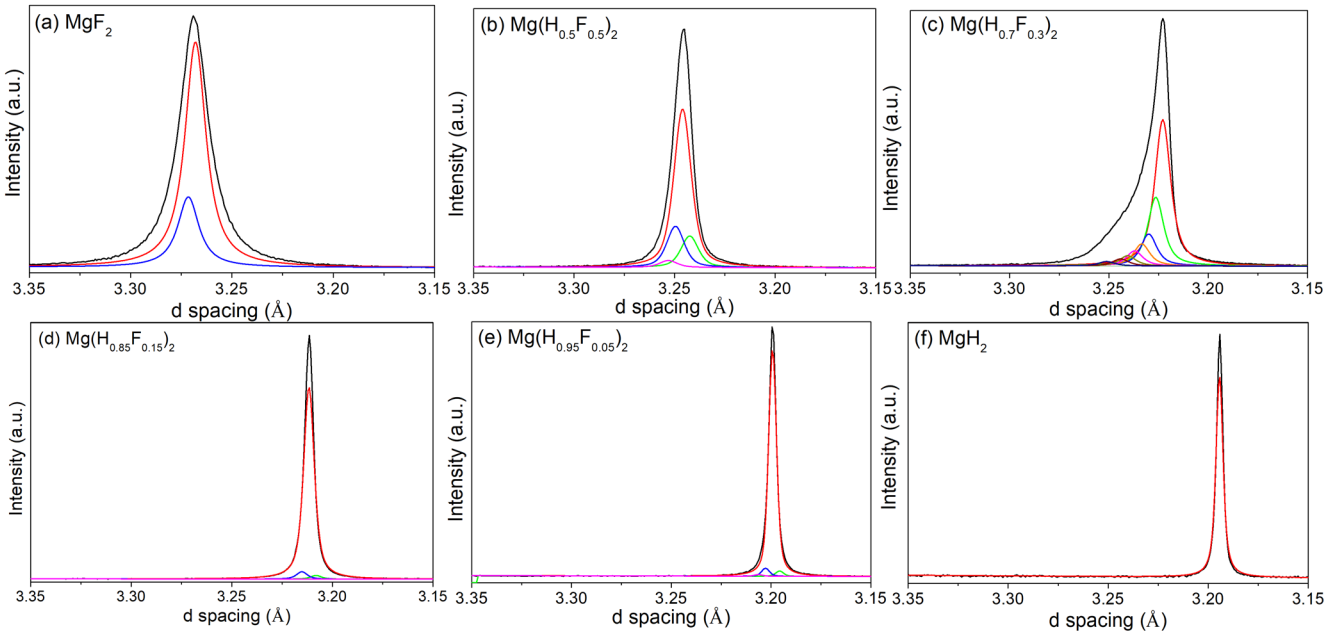

Figure 2. Phase distribution in $Mg(H_xF_{1-x})_2$ solid solutions determined by SR-XRD as observed at the (110) Bragg peak. $T = 27$ °C.

$Mg(H_xF_{1-x})_2$ structure phases (11 for $MgH_{0.85}F_{0.15}$) were refined allowing the lattice parameters to refine freely and H/F occupancy was calculated from the lattice parameters assuming Vegards Law.[41] The fractional atomic coordinate of H/F in the 4*f* position was fixed at 0.303 as it did not move significantly during refinement.

Table 2 details the weight averaged lattice parameters, while Figure 2 illustrates the data by focusing on the (110) Bragg peak. The lattice parameters of each phase are detailed in Table S1) Phase segregation is apparently minimal for all samples, which is in contrast with a recent study on NaH_xF_{1-x} ($x = 1$, 0.95, 0.85, 0.70, 0.50, 0), where a statistical distribution of phases was observed after annealing for 6 days.[42] The only sample exhibiting a large dispersion of phases was $Mg(H_{0.70}F_{0.3})_2$, which is most likely due to insufficient annealing during synthesis. The tail of the peak tends towards higher *d* spacing of which is indicative of a large spread of phases with increased F^- content.

Each of these solid solutions was modelled using DFT in order to complement the XRD and INS data. The optimised DFT supercells were first analysed to ensure that the unit cell parameters and bond distances agreed with the experimental data. Table S2 details the unit cell volumes, lattice parameters and bond distances for the supercells and compares them to the experimental data. For each of the parameters a similar trend observed between the calculated and measured data sets. In addition, each of the respective experimental and theoretical data sets agree to within 3.1%, of which the largest deviation is for the MgF_2 unit cell volume. Overall, the significant agreement suggests that the calculated DFT data represents a quality model to fit against the INS data.

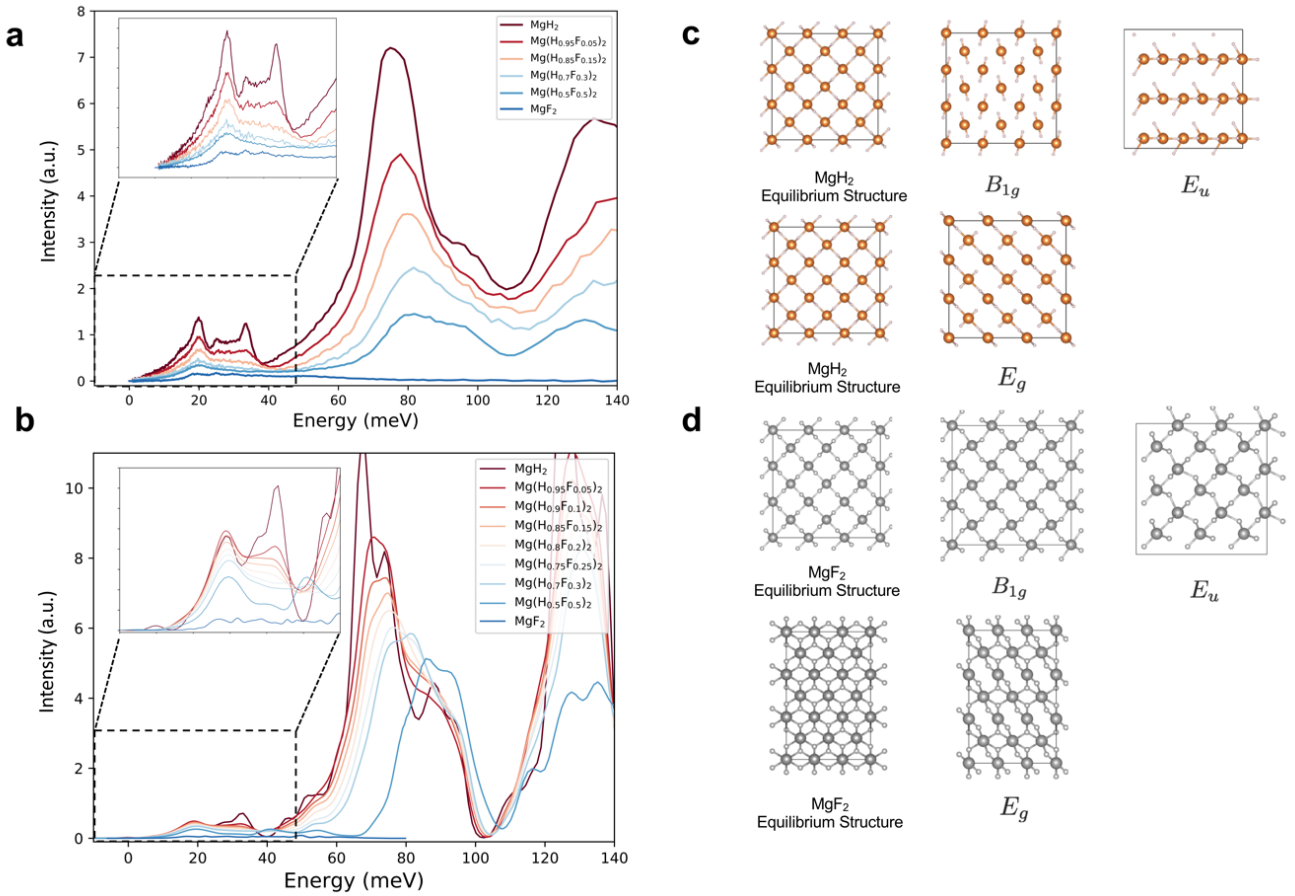

Figure 3. Phonon density-of-states of $Mg(H_xF_{1-x})_2$ solid solutions determined by (a) INS (intensity is normalised) and (b) DFT-based lattice dynamic calculations. For calculated data the contributions from different constituent atoms are weighted by their corresponding *inelastic* neutron scattering cross-sections. For MgF_2, there are no phonon branches beyond 80 meV. Insets show the enlarged low-energy part of the phonon density-of-states. (c-d) show the pattern of atomic vibrations for the B_{1g}, E_u and E_g phonon modes for MgH_2 and MgF_2.

3.2. Inelastic Neutron Spectroscopy The INS spectra, for each of the Mg−H−F compositions, were measured to determine the similarities in the structural dynamics between the solid solutions and pure components (Figure 3). The spectrum for MgH_2 agrees with previously reported ones.[17, 18] There are three low intensity vibrations below 40 meV at 20, 25 and 33 (B_{1g}) meV, which have been previously ascribed primarily to in-phase vibrations of hydrogen atoms with in-phase vibrations of the Mg atoms (lattice vibrations).[17] The broad mode between 60 − 105 meV is described as H-related E_u optic modes, which are three-fold degenerated, and the large widths suggest a large dispersion of the optic phonon branches and consequently strong H–H interactions.[17] Above 105 meV, a very broad region is observed that is attributed to the E_g mode, which is a two-fold degenerate mode that corresponds to the asymmetric bending of the H(F)−Mg−H(F) bond (equatorial) in the [001] plane parallel to the *c*-axis.[43] A schematic illustration of these three vibrational modes for MgH_2 and MgF_2 is shown in Figures 3(c) and 3(d). To complement the INS results, DFT-based lattice dynamics were applied to model the generalised phonon density-of-states (GDOS). Upon weighting the results with the inelastic neutron scattering cross-sections for different elements, Figure 3(b) shows an excellent agreement between theoretical GDOS and INS spectrum for MgH_2. This validates our theoretical calculations, which allows us to extract useful information for understanding the influence of F^- doping on the lattice dynamics for the systems as probed by the INS experiments. Notice that under harmonic approximations, GDOS for MgH_2 shows a small non-vanishing GDOSat negative phonon energies, suggesting that MgH_2 is anharmonic and thus MgH_2 is thermally stabilised at 300 K. Such a feature is not observed in all F^- doped structures.

As F^- content in the solid solution increases, a number of changes to the INS spectra are observed. The vibration at 33 meV becomes broader and almost vanishes along with the peak at 25 meV, while the vibration at 20 meV remains. This can be attributed to the fact that the B_{1g} mode for MgF_2 is much softer than that of MgH_2, which occurs at around 9.1 meV, as revealed by lattice dynamic calculations. The most intense peak at 75 meV gradually shifts to higher energy with higher F^- content, to 83 meV for $MgH_{0.50}F_{0.50}$, which also agrees well with GDOS obtained from lattice dynamic calculations. Atomic vibrations within this energy range are typically dominated by the optical E_u modes Figure 3(c) arising from the vibrations of H sublattices, an upshift in the energy thus indicates this mode is significantly stiffened by the addition of fluorine in the system. Such a shift in the frequencies of optical phonon reflects the enhancement of ionicity in the $Mg(H_xF_{1-x})_2$ with increasing fluoride content, as F^- is of larger electronegativity to hydrogen, which consequently draws more electrons from Mg compared to H^-.

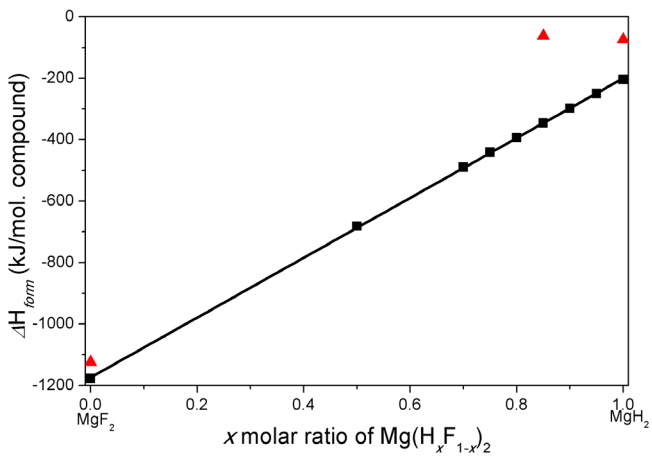

Figure 4. Formation energies for $Mg(H_xF_{1-x})_2$. Black squares correspond to DFT calculated formation energies, red triangles correspond to experimentally derived formation energies.[7, 10, 44]

3.3. Thermodynamics of $Mg(H_xF_{1-x})_2$ DFT modelling enables the extraction of more information than just the phonon density-of-states, with formation energy (ΔH_{form}) of $Mg(H_xF_{1-x})_2$ solid solutions being an indicator for material stability. Figure 4 and Table S3 illustrate a linear trend with ΔH_{form} becoming more negative as the concentration of F^- increases in $Mg(H_xF_{1-x})_2$. As such, the theoretical ΔH_{form} for MgH_2 and MgF_2 is −204 and −1178 kJ/mol of compound, respectively. This indicates that as F^- substitution increases so does the thermal stability of the compound.

Experimental thermodynamic data do not mirror this trend. Although the experimental and DFT calculated ΔH_{form} for MgF_2 differs by only 4.5% (experimental ΔH_{form} = −1124 kJ/mol of compound),[44] the DFT value for MgH_2 is 175% the magnitude of the experimentally determined value of −74.06 ± 0.42 kJ/mol.[7] These two data points do suggest that ΔH_{form} becomes more negative with F^- content, but the experimental value for $Mg(H_{0.85}F_{0..15})_2$ of −62.6 ± 0.2 kJ/mol does not follow a linear trend and actually becomes less negative compared to MgH_2.

The experimental ΔH_{form} for MgH_2 and $Mg(H_{0.85}F_{0..15})_2$ is derived from the enthalpy of hydrogen desorption (ΔH_{des}) determined by PCI (Pressure–concentration isotherm) analysis. Therefore an assumption must be made in that there is no pressure hysteresis between the absorption and desorption process. For these particular materials, hysteresis has been shown not to occur and any artefact is likely due to the slow kinetics of the reaction process.[7, 10] As such these values can be expressed as ΔH_{form}. Pressure–concentration isotherm (PCI) analysis is the ideal method to determine the thermodynamics associated with the reaction of hydrogen release, in which the enthalpic and entropic contributions can be individually identified using a van't Hoff plot.[45] Unfortunately, PCI analysis has only been conducted on pure MgH_2 (ΔH_{des} = 74.06 ± 0.42 kJ/mol; ΔS_{des} = 133.4 ± 0.7 J/K/mol)[7] and $Mg(H_{0.85}F_{0..15})_2$ (ΔH_{des} = 62.6 ± 0.2 kJ/mol ; ΔS_{des} = 111.5 ± 0.2 J/K/mol).[10] Although at first glance, the magnitude of ΔH_{des} and ΔS_{des} are both observed to decrease with increasing F^- content, which seems to be counterintuitive when claiming the system is becoming stabilised. However, the magnitude of ΔS_{des} decreases to a larger extent than the magnitude of ΔH_{des}, resulting in ΔG_{des} becoming less-negative as F^- content increased, implying that decomposition will occur at higher temperatures when under the same back pressure of H_2. In short, ΔS_{des} has a larger impact on the temperature of decomposition than ΔH_{des}.

The difference between the DFT and experimentally determined enthalpy of formation may be attributed to the reaction pathways employed when determining ΔH_{form}. DFT calculations assume direct formation from the elements, whereas the measured values are determined based on the reversible reaction displayed in equation (2). The endothermic ΔH_{des} determined by PCI experiments includes the formation of pure MgF_2 of which is an exothermic reaction. Therefore, the exothermic formation of additional Mg−F bonds reduces the overall measured ΔH_{des}. During the formation of $Mg(H_xF_{1-x})_2$ from MgF_2 + Mg the endothermic contribution encountered during the breaking of Mg−F bonds therefore decreases the ΔH_{form} compared to that expected if formed from the elements. As a result, ΔH_{form} determined by DFT calculations would be more negative than those determined experimentally.

The increased thermal stability with increasing F^- content has been demonstrated using DSC-TGA and as such the temperature of decomposition is a better measure of thermal stability than using ΔH_{form} calculated using DFT alone. In this study, ΔH_{form} was calculated at 0 K and therefore it is impossible to estimate the temperature of decomposition using these calculations, although it does provide a good qualitative estimate of stability. ΔS_{form} must be calculated in order to determine the temperature of formation/decomposition. The enthalpy and entropy determined by PCI analysis the temperature of formation under 1 bar H_2 to be 282 and 288 °C for MgH_2 and $MgH_{0.85}F_{0.15}$, respectively ($\Delta G = \Delta H - T\Delta S$, where $\Delta G = 0$).

3.4. Thermal Transport Properties of $Mg(H_xF_{1-x})_2$ If these $Mg(H_xF_{1-x})_2$ compounds are to be implemented as thermal energy storage materials, the thermal properties must be determined. The thermal transport properties of the $Mg(H_xF_{1-x})_2$ compounds are presented in Table 3. A non-linear relationship exists between the thermal transport properties and amount of H/F present (Figure 5). The data collected for MgF_2 of 0.676(6) W/m.K is lower than that measured in the literature of 11.6 W/m.K.[46] The measurement of thermal transport properties are highly susceptible towards sample preparation and measurement conditions, in this study the samples were measured as a pelletised powder (370 MPa), while a pre-melted MgF_2 pellet was used previously leading to an increased λ_{TC}. The results provided here are all self-consistent and comparable due to the identical sample preparation.

The thermal conductivity of MgH_2 was measured in this study as 2.08(3) W/m.K, where k = 1.53(7) mm²/s and C = 1.37(8) MJ/m³·K. λ_{TC} measured in this study is therefore reasonably close with literature values of 0.40 – 1.21 W/m.K.[21, 47, 48] The literature values were obtained from samples measured as a pellet pressed at a pressure of 100 MPa with a λ_{TC} = 0.70 W/m·K being determined,[21] while additional cold rolling enabled a measurement of 1.21 W/m.K.[48] The variation in results is therefore attributed to the effect of sample preparation conditions. Thermal properties are enhanced by phonon interactions,[49] hence smaller particle size, increased pressure and pre-melting enhance thermal transport properties. The sample measurements in this study were conducted under identical conditions under an Ar atmosphere. Thermal conductivity and diffusivity decrease with increasing F^- content, and is at a minima for $MgH_{0.5}F_{0.5}$, before a slight increase is observed for MgF_2. The heat capacity per unit volume of these materials appears to vary between 1.17(4) and 1.58(3) MJ/m³·K with a specific trend not

being observed. In fact, the values for the F^- containing materials may be considered as being almost equivalent within error.

Overall, the λ_{TC} for these F-substituted materials are highly comparable to other metal hydride materials. For instance λ_{TC} = 0.96 W/m·K for $NaBH_4$,[50] and 0.06 – 4.5 W/m·K for $NaAlH_4$

Table 3. Thermal Transport Properties of $Mg(H_xF_{1-x})_2$ measured at room temperature under Ar atmosphere. λ_{TC} is thermal conductivity (W/m.K), k is thermal diffusivity (mm^2/s), and C is the heat capacity per unit volume ($MJ/m^3.K$).

	λ_{TC} [W/m·K]	K [mm^2/s]	C [$MJ/m^3·K$]
MgH_2	2.08(3)	1.53(7)	1.37(8)
$MgH_{0.95}F_{0.05}$	1.297(6)	0.98(4)	1.32(5)
$MgH_{0.85}F_{0.15}$	0.717(3)	0.49(1)	1.46(3)
$MgH_{0.70}F_{0.30}$	0.584(2)	0.42(1)	1.39(3)
$MgH_{0.50}F_{0.50}$	0.481(3)	0.41(2)	1.17(4)
MgF_2	0.676(6)	0.43(1)	1.58(3)

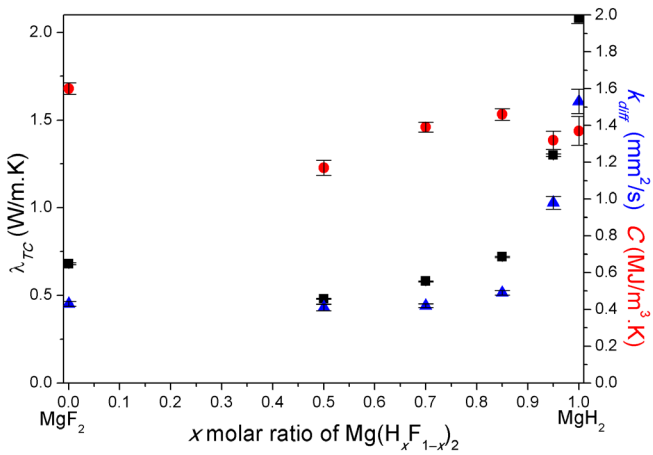

Figure 5. Thermal transport properties of $Mg(H_xF_{1-x})_2$. Thermal conductivity (black square), thermal diffusivity (blue triangle) and volumetric heat capacity (red circle) measured at RT under Ar atmosphere.

depending on conditions.[51, 52] It was determined that an optimal value of ~5 W/m.K for a hydrogenated sample of $LaNi_{4.9}Al_{0.3}$ allows for optimal hydrogen absorption kinetics, while a larger value only has a minor incremental influence.[53] Therefore, to gain technological application, it may be beneficial to enhance λ_{TC} by the addition a material such as exfoliated natural graphite.[9, 21]

4. CONCLUSIONS

This study has detailed a thorough characterisation of fluorine substituted magnesium hydride ($Mg(H_xF_{1-x})_2$ where x = 1, 0.95, 0.85, 0.70, 0.50, 0), a class of materials that have potential application as hydrogen storage or thermal energy storage materials. The physical properties of these solid solutions have been studied by powder X-ray diffraction, inelastic neutron spectroscopy, and thermal conductivity. In addition, these measurements have been verified by density functional theory calculations.

Using these techniques, a number of trends have been identified that can be correlated to the random substitution of F^- into the crystal lattice. The tetragonal unit cell volume expands in a quadratic trend by 5.4 % from MgH_2 to MgF_2. This expansion is isotropic in nature with a 2.3 % expansion in the *a*-axis compared to *c*-axis. This is mirrored with a preferred extension of the axial Mg−H(F) bond distances over the equatorial bond distances. Overall, the addition of F^- increases the average Mg−H(F) bond strength, which increases the thermal stability of the material, making fluorine rich Mg−H−F compounds efficient thermal energy storage materials. Despite the reduction in hydrogen-storage capacity, the increased thermal stability will permit hydrogen cycling at higher temperatures and therefore greater efficiency for thermal energy storage.

Inelastic neutron diffraction data has been collected for the first time for fluorine substituted magnesium hydride. Along with the simulated GDOS data from density functional theory calculations, these materials have exhibited a trend in vibrational frequencies and intensities from MgH_2 towards MgF_2 that is in line with the expansion in lattice parameters and bond distances.

The thermal transport properties, including thermal conductivity, diffusivity and heat capacity, for the range of $Mg(H_xF_{1-x})_2$ samples was also determined. This was the first time that MgH_2 and MgF_2 have been measured under the same conditions which has allowed a direct comparison with the fluorine substituted analogues.

ASSOCIATED CONTENT

Supporting Information.
Quantitative Rietveld analysis of SR-XRD data for $Mg(H_xF_{1-x})_2$ solid solutions; thermodynamic and crystallographic parameters derived from DFT calculations; NEXAFS experimental, results and discussion.
This material is available free of charge via the Internet at http://pubs.acs.org."

AUTHOR INFORMATION

Corresponding Author

* E-mail: terry_humphries81@hotmail.com

Author Contributions

All authors have given approval to the final version of the manuscript.

Notes

The authors declare no competing financial interest.

ACKNOWLEDGMENT

The authors CEB, TDH, MVS and MP acknowledge the financial support of the Australian Research Council (ARC) for ARC Linkage grants LP120101848 and LP150100730. CEB, TDH, MP and MVS acknowledge financial support from the Department of Industry Innovation and Science for the 2019 Global Innovation Linkage (GIL73589) grant. CEB and MP acknowledge the financial support of the ARC for DP150101708. MP acknowledges his ARC Future Fellowship FT160100303. JY acknowledge the support from ANSTO for a Postdoctoral Fellowship. The authors also acknowledge funding from the ANSTO, which enabled research at the powder diffraction beamline at the Australian Synchrotron and Inelastic Neutron Spectroscopy to be undertaken on Pelican. The authors would also like to acknowledge Dr J.P. Veder for collecting the NEXAFS data.

REFERENCES

1. Züttel, A.; Remhof, A.; Borgschulte, A.; Friedrichs, O., Hydrogen: the future energy carrier. *Phil. Trans. R. Soc. A* **2010,** *368* (1923), 3329-3342.

2. Makepeace, J. W.; He, T.; Weidenthaler, C.; Jensen, T. R.; Chang, F.; Vegge, T.; Ngene, P.; Kojima, Y.; de Jongh, P. E.; Chen, P.; David, W. I. F., Reversible ammonia-based and liquid organic hydrogen carriers for high-density hydrogen storage: Recent progress. *Int. J. Hydrogen Energy* **2019,** *44* (15), 7746-7767.

3. Crivello, J.-C.; Denys, R. V.; Dornheim, M.; Felderhoff, M.; Grant, D. M.; Huot, J.; Jensen, T. R.; de Jongh, P.; Latroche, M.; Walker, G. S.; Webb, C. J.; Yartys, V. A., Mg-based compounds for hydrogen and energy storage. *Appl. Phys. A* **2016,** *122* (2), 85.

4. Webb, C. J., A review of catalyst-enhanced magnesium hydride as a hydrogen storage material. *J. Phys. Chem. Solids* **2015,** *84*, 96-106.

5. Yartys, V. A.; Lototskyy, M. V.; Akiba, E.; Albert, R.; Antonov, V. E.; Ares, J. R.; Baricco, M.; Bourgeois, N.; Buckley, C. E.; Bellosta von Colbe, J. M.; Crivello, J. C.; Cuevas, F.; Denys, R. V.; Dornheim, M.; Felderhoff, M.; Grant, D. M.; Hauback, B. C.; Humphries, T. D.; Jacob, I.; Jensen, T. R.; de Jongh, P. E.; Joubert, J. M.; Kuzovnikov, M. A.; Latroche, M.; Paskevicius, M.; Pasquini, L.; Popilevsky, L.; Skripnyuk, V. M.; Rabkin, E.; Sofianos, M. V.; Stuart, A.; Walker, G.; Wang, H.; Webb, C. J.; Zhu, M., Magnesium Based Materials for Hydrogen Based Energy Storage: Past, Present and Future. *Int. J. Hydrogen Energy* **2019,** *44* (15), 7809-7859.

6. Humphries, T. D.; Sheppard, D. A.; Buckley, C. E., Recent advances in the 18-electron complex transition metal hydrides of Ni, Fe, Co and Ru. *Coord. Chem. Rev.* **2017,** *342*, 19-33.

7. Paskevicius, M.; Sheppard, D. A.; Buckley, C. E., Thermodynamic changes in mechanochemically synthesized magnesium hydride nanoparticles. *J. Am. Chem. Soc.* **2010,** *132* (14), 5077-5083.

8. DOE Technical targets for onboard hydrogen storage for light-duty vehicles. https://www.energy.gov/eere/fuelcells/doe-technical-targets-onboard-hydrogen-storage-light-duty-vehicles (accessed 19/03/2019).

9. Dong, D.; Humphries, T. D.; Sheppard, D. A.; Stansby, B.; Paskevicius, M.; Sofianos, M. V.; Chaudhary, A. L.; Dornheim, M.; Buckley, C. E., Thermal optimisation of metal hydride reactors for thermal energy storage applications. *Sustain. Energy Fuels* **2017,** *1* (8), 1820-1829.

10. Tortoza, M. S.; Humphries, T. D.; Sheppard, D. A.; Paskevicius, M.; Rowles, M. R.; Sofianos, M. V.; Aguey-Zinsou, K. F.; Buckley, C. E., Thermodynamics and performance of the Mg-H-F system for thermochemical energy storage applications. *Phys. Chem. Chem. Phys.* **2018,** *20* (4), 2274-2283.

11. Pinatel, E. R.; Corno, M.; Ugliengo, P.; Baricco, M., Effects of metastability on hydrogen sorption in fluorine substituted hydrides. *J. Alloys Compd.* **2014,** *615*, S706-S710.

12. Varunaa, R.; Ravindran, P., Phase stability, phase mixing, and phase separation in fluorinated alkaline earth hydrides. *J. Phys. Chem. C* **2017,** *121* (40), 21806-21820.

13. Bortz, M.; Bertheville, B.; Böttger, G.; Yvon, K., Structure of the high pressure phase γ-MgH2 by neutron powder diffraction. *Journal of Alloys Compounds* **1999,** *287* (1-2), L4-L6.

14. Corey, R. L.; Ivancic, T. M.; Shane, D. T.; Carl, E. A.; Bowman, R. C.; Bellosta von Colbe, J. M.; Dornheim, M.; Bormann, R.; Huot, J.; Zidan, R.; Stowe, A. C.; Conradi, M. S., Hydrogen motion in magnesium hydride by NMR. *J. Phys. Chem. C* **2008,** *112* (49), 19784-19790.

15. Senegas, J.; Pezat, M.; Darnaudery, J. P.; Darriet, B., Study by NMR on localization and movements of protons in MgH_2 and Mg_2NiH_4 hydrides. *J. Phys. Chem. Solids* **1981,** *42* (1), 29-35.

16. Felsteiner, J.; Heilper, M.; Gertner, I.; Tanner, A. C.; Opher, R.; Berggren, K. F., Compton scattering study of the electronic structure of magnesium hydride. *Phys. Rev. B* **1981,** *23* (10), 5156-5162.

17. Santisteban, J. R.; Cuello, G. J.; Dawidowski, J.; Fainstein, A.; Peretti, H. A.; Ivanov, A.; Bermejo, F. J., Vibrational spectrum of magnesium hydride. *Phys. Rev. B* **2000,** *62* (1), 37-40.

18. Schimmel, H. G.; Johnson, M. R.; Kearley, G. J.; Ramirez-Cuesta, A. J.; Huot, J.; Mulder, F. M., The vibrational spectrum of magnesium hydride from inelastic neutron scattering and density functional theory. *Mater. Sci. Eng. B.* **2004,** *108* (1-2), 38-41.

19. Schimmel, H. G.; Johnson, M. R.; Kearley, G. J.; Ramirez-Cuesta, A. J.; Huot, J.; Mulder, F. M., Structural information on ball milled magnesium hydride from vibrational spectroscopy and ab-initio calculations. *J. Alloys Compd.* **2005,** *393* (1), 1-4.

20. Hanada, N.; Ichikawa, T.; Isobe, S.; Nakagawa, T.; Tokoyoda, K.; Honma, T.; Fujii, H.; Kojima, Y., X-ray absorption spectroscopic study on valence state and local atomic structure of transition metal oxides doped in MgH_2. *J. Phys. Chem. C* **2009,** *113* (30), 13450-13455.

21. Chaise, A.; de Rango, P.; Marty, P.; Fruchart, D.; Miraglia, S.; Olivès, R.; Garrier, S., Enhancement of hydrogen sorption in magnesium hydride using expanded natural graphite. *Int. J. Hydrogen Energy* **2009,** *34* (20), 8589-8596.

22. Shim, J.-H.; Park, M.; Lee, Y. H.; Kim, S.; Im, Y. H.; Suh, J.-Y.; Cho, Y. W., Effective thermal conductivity of MgH_2 compacts containing expanded natural graphite under a hydrogen atmosphere. *Int. J. Hydrogen Energy* **2014,** *39* (1), 349-355.

23. Wallwork, K. S.; Kennedy, B. J.; Wang, D., The High Resolution Powder Diffraction Beamline for the Australian Synchrotron. *Synchrotron Radiation Instrumentation, Pts 1 and 2* **2007,** *879* (1), 879-+.

24. Schmitt, B.; Bronnimann, C.; Eikenberry, E. F.; Gozzo, F.; Hormann, C.; Horisberger, R.; Patterson, B., Mythen Detector System. *Nucl Instrum Meth A* **2003,** *501* (1), 267-272.

25. Young, R. A.; Young, R. A., *The Rietveld Method*. Oxford University Press: 1995.

26. Loopstra, B. O.; Rietveld, H. M., The structure of some alkaline-earth metal uranates. *Acta Crysta. B* **1969,** *25* (4), 787-791.

27. Coelho, A. A., TOPAS and TOPAS-Academic: An optimization program integrating computer algebra and crystallographic objects written in C Plus. *J. Appl. Crystallogr.* **2018,** *51* (1), 210-218.

28. Richard, D.; Ferrand, M.; Kearley, G. J., Analysis and visualisation of neutron-scattering data. *J. Neutron Res.* **1996,** *4* (1-4), 33-39.

29. Mutka, H.; Koza, M. M.; Johnson, M. R.; Hiroi, Z.; Yamaura, J.-I.; Nagao, Y., Generalized density-of-states and anharmonicity of the low-energy phonon bands from coherent inelastic neutron scattering response in the pyrochlore osmates AOs_2O_6 (A = K, Rb, Cs). *Phys. Rev. B* **2008,** *78* (10), 104307.

30. Kresse, G.; Furthmuller, J., Efficient iterative schemes for ab initio total-energy calculations using a plane-wave basis set. *Phys. Rev. B* **1996,** *54* (16), 11169-11186.

31. Perdew, J. P.; Burke, K.; Ernzerhof, M., Generalized gradient approximation made simple. *Phys. Rev. Lett.* **1996,** *77* (18), 3865-3868.

32. Kresse, G.; Joubert, D., From ultrasoft pseudopotentials to the projector augmented-wave method. *Phys. Rev. B* **1999,** *59* (3), 1758-1775.

33. Togo, A.; Tanaka, I., First principles phonon calculations in materials science. *Scr. Mater.* **2015,** *108*, 1-5.

34. Bansal, D.; Hong, J.; Li, C. W.; May, A. F.; Porter, W.; Hu, M. Y.; Abernathy, D. L.; Delaire, O., Phonon anharmonicity and negative thermal expansion in SnSe. *Phys. Rev. B* **2016,** *94* (5), 054307.

35. NIST Center for Neutron Research. https://www.ncnr.nist.gov/resources/n-lengths/list.html (accessed November 2, 2019).

36. Baur, W. H., The rutile type and its derivatives. *Crystallography Reviews* **2007,** *13* (1), 65-113.

37. Haines, J.; Léger, J. M.; Gorelli, F.; Klug, D. D.; Tse, J. S.; Li, Z. Q., X-ray diffraction and theoretical studies of the high-pressure structures and phase transitions in magnesium fluoride. *Phys. Rev. B* **2001,** *64* (13), 134110.

38. Ramesh Babu, K.; Bheema Lingam, C.; Auluck, S.; Tewari, S. P.; Vaitheeswaran, G., Structural, thermodynamic and optical properties of MgF2 studied from first-principles theory. *J. Solid State Chem.* **2011,** *184* (2), 343-350.

39. Noritake, T.; Aoki, M.; Towata, S.; Seno, Y.; Hirose, Y.; Nishibori, E.; Takata, M.; Sakata, M., Chemical bonding of hydrogen in MgH2. *Appl. Phys. Lett.* **2002,** *81* (11), 2008-2010.

40. Vidal, J. P.; Vidal-Valat, G.; Galtier, M.; Kurki-Suonio, K., X-ray study of the charge distribution in MgF2. *Acta Crystallogr A* **1981,** *37* (6), 826-837.

41. Denton, A. R.; Ashcroft, N. W., Vegard's law. *Phys. Rev. A* **1991,** *43* (6), 3161-3164.

42. Humphries, T. D.; Sheppard, D. A.; Rowles, M. R.; Sofianos, M. V.; Buckley, C. E., Fluoride Substitution in Sodium Hydride for Thermal Energy Storage Applications. *J. Mater. Chem. A* **2016,** *4* (31), 12170-12178.

43. Gangrade, A. S.; Varma, A. A.; Gor, N. K.; Shriniwasan, S.; Tatiparti, S. S. V., The dehydrogenation mechanism during the incubation period in nanocrystalline MgH 2. *Phys. Chem. Chem. Phys.* **2017,** *19* (9), 6677-6687.

44. Cox, J. D.; Wagman, D. D.; Medvedev, V. A., *CODATA key values for thermodynamics*. Hemisphere Pub. Corp.: New York, 1989.

45. Sheppard, D. A.; Paskevicius, M.; Buckley, C. E., Thermodynamics of hydrogen desorption from $NaMgH_3$ and its application as a solar heat storage medium. *Chem. Mater.* **2011,** *23* (19), 4298-4300.

46. Koyama, K., Thermal conductivity of magnesium fluoride between 25° and 900°C. *J. Am. Ceram. Soc.* **1969,** *52* (4), 222-224.

47. Camirand, C. P., Measurement of thermal conductivity by differential scanning calorimetry. *Thermochim. Acta* **2004,** *417* (1), 1-4.

48. Lang, J.; Eagles, M.; Conradi, M. S.; Huot, J., Hydrogenation rate limiting step, diffusion and thermal conductivity in cold rolled magnesium hydride. *J. Alloys Compd.* **2014,** *583*, 116-120.

49. Kittel, C.; McEuen, P.; McEuen, P., *Introduction to solid state physics*. Wiley New York: 1976; Vol. 8.

50. Sundqvist, B.; Andersson, O., Thermal conductivity and phase diagrams of some potential hydrogen storage materials under pressure. *Int. J. Thermophys.* **2009,** *30* (4), 1118-1129.

51. Beattie, S. D.; Harris, A.; Levchenko, A.; Rudolph, J.; Willson, C. D.; McGrady, G. S., Thermal conductivity and specific heat measurements of metal hydrides. In *ITCC Proceedings*, 2009; Vol. 11.

52. Sulic, M.; Cai, M.; Kumar, S., Cycling and engineering properties of highly compacted sodium alanate pellets. *Int. J. Hydrogen Energy* **2012,** *37* (20), 15187-15195.

53. Choi, H.; Mills, A. F., Heat and mass transfer in metal hydride beds for heat pump applications. *Int. J. Heat Mass Transfer* **1990,** *33* (6), 1281-1288.

TOC Graphic

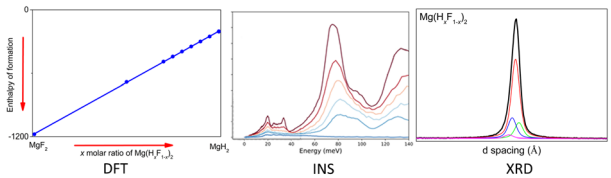

$$x\mathrm{MgH_2} + 1{-}x\mathrm{MgF_2} \rightarrow \mathrm{Mg(H}_x\mathrm{F}_{1-x})_2$$